Nanoelectronics and Its New Materials – A NEW ERA OF NANOSCIENCE

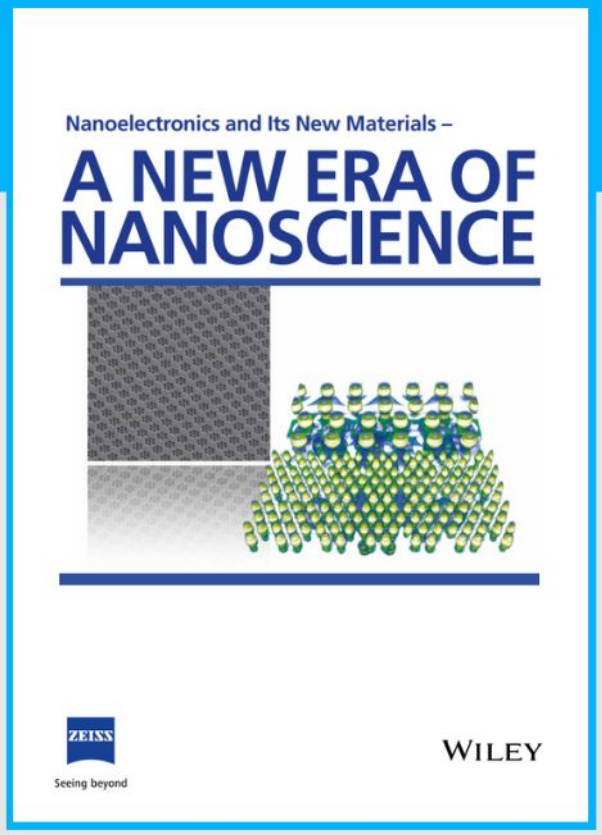

Discover the recent advances in electronics research and fundamental nanoscience.

Nanotechnology has become the driving force behind breakthroughs in engineering, materials science, physics, chemistry, and biological sciences. In this compendium, we delve into a wide range of novel applications that highlight recent advances in electronics research and fundamental nanoscience. From surface analysis and defect detection to tailored optical functionality and transparent nanowire electrodes, this eBook covers key topics that will revolutionize the future of electronics.

To get your hands on this valuable resource and unleash the power of nanotechnology, simply download the eBook now. Stay ahead of the curve and embrace the future of electronics with nanoscience as your guide.

ZEISS

Seeing beyond

WILEY

ADVANCED FUNCTIONAL MATERIALS
www.afm-journal.de

Boosting STE and Nd^{3+} NIR Luminescence in $Cs_2AgInCl_6$ Double Perovskite via Na^+/Bi^{3+}-Induced Local Structure Engineering

Shilin Jin, He Yuan, Tao Pang, Manjia Zhang, Youwu He, Bin Zhuang, Tianmin Wu,* Yuanhui Zheng, and Daqin Chen**

Currently, lanthanide (Ln^{3+}) doped Pb-free double perovskites (DPs) suffer from competitive emissions of the self-trapped exciton (STE) and Ln^{3+}. Herein, a new type of Nd^{3+}-doped $Cs_2AgInCl_6$ DPs with Na^+/Bi^{3+} co-alloying is developed. Benefiting from Na^+/Bi^{3+}-induced local structural modification, both STE broadband visible luminescence and Nd^{3+} near-infrared (NIR) emissions are boosted via free exciton sensitization. Specifically, a total 648-fold enhancement in emitting intensities compared to the Na^+/Bi^{3+}-free counterpart is realized, with a significantly improved NIR photoluminescence quantum yield (PLQY) from 0.16% to 30.3%. First-principles density functional theory calculations, Raman spectra, and steady/transient-state PL spectra verify the modification of local site symmetry, breakdown of parity-forbidden absorption, and reduction of electron-phonon coupling via Na^+/Bi^{3+} doping. Finally, a compact vis–NIR broadband light-emitting diode (LED) is designed by coupling the Na/Bi/Nd: $Cs_2AgInCl_6$ DP with a commercial ultraviolet LED chip, which shows promising applications in spectroscopic analyses and multifunctional lighting.

1. Introduction

Ultra-broadband light sources emitting over vis–NIR's wide spectral range are of great interest in diverse fields. Traditionally, Bi^{3+} doped phosphors can produce UV and visible broadband emissions but are hard to yield NIR emissions.[1] Cr^{3+}-doped phosphors have been regarded as desirable NIR emitters, but most reported Cr^{3+} luminescence is actually located within the far-red region rather than NIR one (especially for emitting wavelength over 1000 nm).[2] In addition, the preparation of phosphors containing Bi^{3+} and Cr^{3+} can be accompanied by the production of Bi^+, Bi^{2+}, Cr^{5+}, and Cr^{6+},[2a,3] which makes the system complex. On the other hand, Ln^{3+} doping enables them to emit a broad spectrum covering from UV to infrared benefiting their plentiful metastable excited levels. For instance, Er-doped, Pr-doped, and Tm-doped broadband NIR-emitting fiber amplifiers have been successfully commercialized. Unfortunately, Ln^{3+}-doped NIR emitters generally suffer from narrowband spectral characteristics and weak 4f-4f intra-transition absorption. To address these issues, sensitizing Ln^{3+} luminescence via semiconductor is expected to be an effective strategy to realize efficient vis–NIR emissions owing to efficient band-to-band absorption and tunable bandgaps.[4]

S. Jin, H. Yuan, M. Zhang, B. Zhuang, D. Chen
College of Physics and Energy
Fujian Normal University
Fuzhou, Fujian 350117, P. R. China
E-mail: dqchen@fjnu.edu.cn

T. Pang
Huzhou Key Laboratory of Materials for Energy Conversion and Storage
College of Science
Huzhou University
Huzhou, Zhejiang 313000, P. R. China

Y. He, T. Wu
Key Laboratory of Opto-Electronic Science and Technology for Medicine of Ministry of Education
College of Photonic and Electronic Engineering
Fujian Normal University
Fuzhou, Fujian 350117, P. R. China
E-mail: ywhe@fjnu.edu.cn; wtm@fjnu.edu.cn

Y. Zheng, D. Chen
Fujian Science & Technology Innovation Laboratory for Optoelectronic Information
Fuzhou, Fujian 350116, P. R. China

Y. Zheng
College of Chemistry
Fuzhou University
Fuzhou, Fujian 350116, P. R. China

D. Chen
Fujian Provincial Collaborative Innovation Center for Advanced High-Field Superconducting Materials and Engineering
Fuzhou, Fujian 350117, P. R. China

D. Chen
Fujian Provincial Engineering Technology Research Center of Solar Energy Conversion and Energy Storage
Fuzhou, Fujian 350117, P. R. China

The ORCID identification number(s) for the author(s) of this article can be found under https://doi.org/10.1002/adfm.202304577

DOI: 10.1002/adfm.202304577

All-inorganic lead halide perovskite semiconductors have been extensively studied for their promising application prospects in optoelectronic fields.[5] Especially, the advantages of facile synthesis, tunable and high-purity emissions, as well as eminent PLQYs enable them to find applications in LEDs and high-definition displays.[6] However, investigations have been predominantly limited to the visible spectral range so far.[7] In this case, great efforts have been devoted to extending the spectral region of metal halide perovskites to the NIR range for a variety of new applications. Recently, doping Ln^{3+} ions was proposed to confer and tune the optical properties of halide perovskites.[8] Accordingly, NIR luminescence of Yb^{3+} with PLQY beyond 100% was achieved in Yb^{3+}-doped $CsPbCl_3$ via quantum-cutting energy transfer from halide perovskite to Yb^{3+} ions.[9] Despite the promising prospects, two key issues of lead toxicity and inherent instability need to be solved. In this regard, lead-free halide DP_S with low toxicity and excellent stability have been considered the ideal hosts for Ln^{3+} doping to produce NIR emissions.[10] Among the DP family, $Cs_2AgInCl_6$ with a direct band gap feature has been extensively studied because of its diverse structural variants with Ag^+ and In^{3+} cations substituted by other alloying ions.[11] Importantly, $Cs_2AgInCl_6$ owns an octahedral coordination environment of $[InCl_6]^{3-}$ suitable for Ln^{3+} incorporation into equivalent In^{3+} sites. Currently, Yb^{3+} and Er^{3+} ions have been successfully incorporated into the $Cs_2AgInCl_6$ host, giving rise to broadband visible luminescence ascribed to STE and NIR emissions originated from f-f transition of Yb^{3+} and Er^{3+} at 996 and 1537 nm.[12] Unfortunately, these Ln^{3+}-doped $Cs_2AgInCl_6$ DP suffer from weak absorption/excitation of $Cs_2AgInCl_6$ DP and competitive emissions between STE and Ln^{3+} dopants owing to the dominant STE sensitization mechanism.[13] Energy transfer from STE to Ln^{3+} dopants will reduce STE luminescence.[10c,13a,14] Therefore, it is urgently demanded to optimize Ln^{3+} doping type and $Cs_2AgInCl_6$ DP structure to effectively boost NIR emissions of Ln^{3+} dopants without STE quenching.

Herein, we report the local structure engineering of Nd^{3+}-doped $Cs_2AgInCl_6$ DP via Na^+/Bi^{3+} co-alloying to produce efficient NIR emissions of Nd^{3+} from 850 to 1400 nm. Nd^{3+} ions own plenty of intermediate energy levels, which can well match the energy band structure of $Cs_2AgInCl_6$ DP and promote efficiently sensitized NIR emissions via free excitons (FEs) rather STEs. Excited-state dynamics and energy transfer mechanism in the $Na^+/Bi^{3+}/Nd^{3+}$ tri-doped $Cs_2AgInCl_6$ DP were systematically studied by virtue of temperature-sensitive steady/transient-state PL spectra as well as femtosecond transient absorption (fs-TA) spectra. Importantly, Na^+/Bi^{3+} co-alloying can simultaneously boost broadband STE luminescence and Nd^{3+} NIR emissions, showing a total 648-fold increase in STE and Nd^{3+} NIR PL intensities compared to the Na-Bi-free counterpart, with a significantly improved NIR PLQY from 0.16% to 30.3%. As tabulated in Table S1, Supporting Information, this is the first report that both STE and Ln^{3+} NIR emissions are concurrently enhanced in the Ln^{3+}-doped DP-derived materials. First-principles density functional theory (DFT) calculations and Raman spectroscopic analysis evidenced that such significant enhanced luminescence is mainly ascribed to the synergistic effect of modification of local site symmetry, breakdown of parity forbidden absorption, reduction of electron-phonon coupling, and energy transfer from free exciton to Nd^{3+}. Furthermore, we construct a phosphor-converted broadband light-emitting device (pc-LED) by coupling it with a commercial UV LED chip and show its potential applications in spectral analysis and night vision.

2. Results and Discussion

$Na^+/Bi^{3+}/Nd^{3+}$ tri-doped $Cs_2AgInCl_6$ samples were prepared by a modified coprecipitation method.[15] **Figure 1**a shows the highly symmetric face-centered cubic structure of $Cs_2AgInCl_6$ DP (space group: Fm $\bar{3}$m), where $[AgCl_6]^{5-}$ and $[InCl_6]^{3-}$ octahedrons alternately occupy the unit cell and Cs^+ ions are located in the middle of the cub-octahedral centers.[16] Na^+ and Bi^{3+}/Nd^{3+} are expected to replace the lattice positions of Ag^+ and In^{3+}, respectively, depending on the ionic equivalent charge and ionic radii (Figure 1a).[17] X-ray diffraction (XRD) patterns for the Nd^{3+} doped, Bi^{3+}/Nd^{3+} co-doped, and $Na^+/Bi^{3+}/Nd^{3+}$ tri-doped samples (Figure 1b) are well assigned to cubic $Cs_2AgInCl_6$ phase (ICSD number 244519). With the doping of Nd^{3+}, Bi^{3+}, and Na^+ ions, the diffraction peaks appear to shift towards smaller angle (Figure S1, Supporting Information), indicating a slight expansion of $Cs_2AgInCl_6$ lattice since Nd^{3+} (r = 0.98 Å, CN = 6) and Bi^{3+} (r = 1.02 Å, CN = 6) ionic radii are larger than the In^{3+} (r = 0.80 Å, CN = 6) and the Na–Cl bond length is longer than the Ag-Cl one.[17] The nominal Nd/In doping ratio was set from 111% to 333%, which corresponds to the actual concentration from 0.97% to 2.03% measured by inductively coupled plasma-mass spectrometry (ICP-MS, Table S2, Supporting Information). Only a tiny fraction of Nd^{3+} ions are incorporated into the DP crystalline lattice, which may be due to highly different electronic configurations of Nd^{3+} and In^{3+} ions.

Scanning electron microscopy (SEM) images show micron-sized crystals with polygonal shapes for four product groups and a slight reduction in crystal size following Nd^{3+}, Bi^{3+}, and Na^+ doping (Figure S2, Supporting Information). The uniform distribution of Cs, Ag, In, Cl, Nd, Bi, and Na elements was confirmed by energy dispersive X-ray (EDX) mapping measurements in Na/Bi/Nd: $Cs_2AgInCl_6$ DP (Figure S3, Supporting Information). Typical Cs 3d, Ag 3d, In 3d, Cl 2p, and Nd 3d signal peaks (Figure S4, Supporting Information) were detected by high-resolution X-ray photoelectron spectroscopy (XPS), and extra Bi 4f and Na 1s peaks were observed for Na/Bi/Nd:$Cs_2AgInCl_6$ DP (Figure S5, Supporting Information). The binding energy of Ag 3d and In 3d are altered after Na^+/Bi^{3+} alloying (Figure S4c,d, Supporting Information). All these results confirm Na^+ and Bi^{3+} ions have entered into the Nd:$Cs_2AgInCl_6$ lattice. The actual elemental contents of Na^+ (≈40 mol%) and Bi^{3+} (≈10 mol%) ions determined from EDX and XPS are consistent with the corresponding stoichiometric ratios (Tables S3 and S4, Supporting Information).

The effect of Na^+/Bi^{3+} co-alloying on Nd^{3+} NIR luminescence was investigated (Figure 1c,d). Besides broadband STE luminescence, all the samples show three typical NIR emission bands assigned to Nd^{3+} $^4F_{3/2} \rightarrow {}^4I_J$ transitions (J = 9/2, 11/2, 13/2: 890, 1063, and 1351 nm, respectively). Apparently, Nd: $Cs_2AgInCl_6$ sample exhibits very weak STE and Nd^{3+} NIR emissions, which will be enhanced by the introduction of Bi^{3+} dopants. Importantly, the co-alloying of Na^+/Bi^{3+} will further improve SET and Nd^{3+} NIR emissions (Figure 1c). The total PL intensities of STE and Nd^{3+} activator in the Bi^{3+}/Nd^{3+} co-doped and $Na^+/Bi^{3+}/Nd^{3+}$ tri-doped DPs are enhanced by 226 and

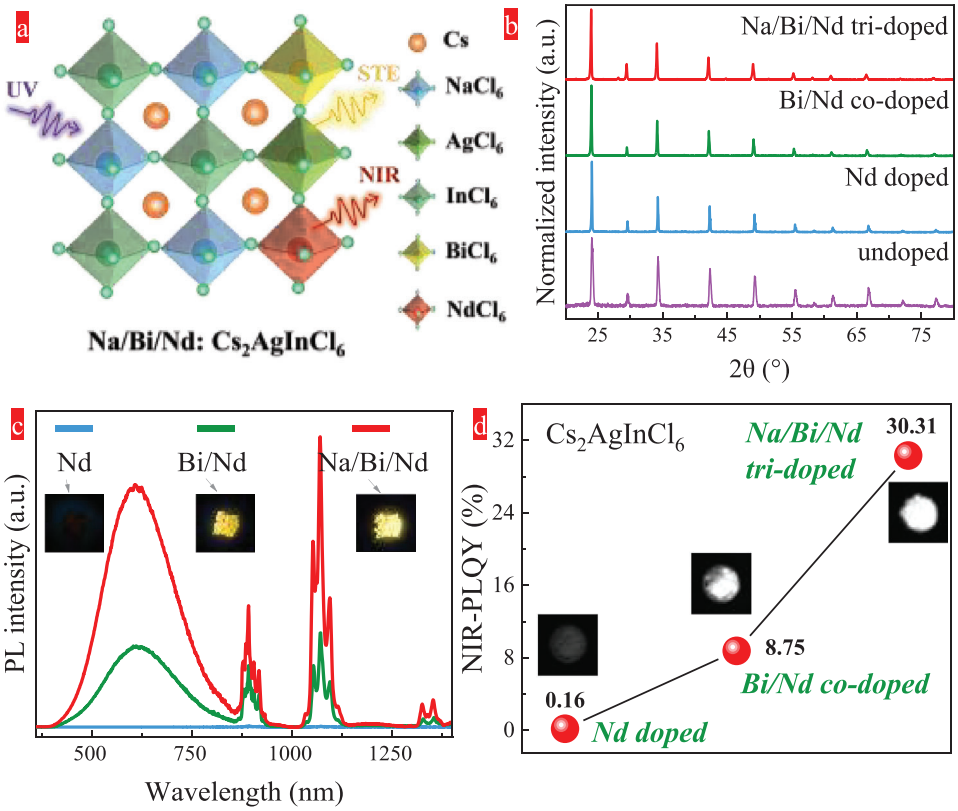

Figure 1. a) Schematic illustration of $Na^+/Bi^{3+}/Nd^{3+}$ tri-doped $Cs_2AgInCl_6$ DP crystal structure. b) XRD patterns, c) PL spectra, and d) NIR PLQY of the Nd^{3+} doped, Bi^{3+}/Nd^{3+} co-doped, and $Na^+/Bi^{3+}/Nd^{3+}$ tri-doped $Cs_2AgInCl_6$ DPs. Insets of (c) and (d) show STE and NIR emitting photographs recorded by visible and NIR cameras, respectively.

648 times, respectively, relative to that of Nd:$Cs_2AgInCl_6$. As evidenced in Figure 1d, NIR PLQYs of the Nd^{3+} doped, Bi^{3+}/Nd^{3+} co-doped and $Na^+/Bi^{3+}/Nd^{3+}$ tri-doped samples are determined to be 0.16%, 8.75%, and 30.31%, respectively. Visible and NIR luminescent images recorded by cameras clearly demonstrate the improved emitting brightness upon Na^+/Bi^{3+} co-alloying (insets of Figure 1c,d). The total PLQY including both STE and NIR bands is 92.57% for the Na/Bi/Nd:$Cs_2AgInCl_6$ DP.

Absorption spectra (**Figure 2**a) of the pristine and Nd:$Cs_2AgInCl_6$ DPs are similar, with strong absorption at ≈320 nm and very weak absorption at ≈370 nm. In addition, the un-doped sample shows an absorption tail starting at longer wavelengths, which is completely eliminated after $Na^+/Bi^{3+}/Nd^{3+}$ doping. Impressively, Bi^{3+} doping leads to significant enhancement of the ≈370 nm absorption band, and the optical absorption behavior is barely altered by further tri-doping Na^+ ions. Therefore, it is believed that this improved absorption at ≈370 nm arises from the contribution of Bi^{3+} dopants, which is important for their application owing to the excitation of commercial UV LED emitted at 360–385 nm light. The optical bandgap of these DPs was found to drop from 3.56 eV in Nd: $Cs_2AgInCl_6$ to 3.02 and 3.07 eV in Bi/Nd:$Cs_2AgInCl_6$ and Na/Bi/Nd:$Cs_2AgInCl_6$ according to the Tauc plots (Figure 2b). PL excitation (PLE) spectra by monitoring STE emission and Nd^{3+} NIR emission (Figure 2c,d) clearly evidence the occurrence of excitation band at ≈370 nm and significantly enhanced excitation intensity upon Na^+/Bi^{3+} doping, which is consistent with the observed absorption (Figure 2a). We detected PL decay curves of STE emission and Nd^{3+} $^4F_{3/2} \rightarrow {}^4I_J$ (J = 9/2, 13/2) transition (Figure 2e,f and Figure S6, Supporting Information). Upon the doping of Na^+/Bi^{3+} ions, the decay lifetimes of STE transition at 610 nm and Nd^{3+} transition at 890 nm increase from 0.19 to 2.03 µs (for STE emission) and 2.25 to 2.99 ms (for Nd^{3+} emission), respectively. The increase in the decay lifetime indicates that the non-radiative decay processes of both STE and Nd^{3+} NIR emissions are suppressed after Na^+/Bi^{3+} incorporation. Generally, the decay lifetime of STE emission exhibits a short lifetime on a microsecond scale due to Jahn–Teller distortion-induced exciton recombination, while PL lifetime for Nd^{3+} emission was millisecond owing to typical parity-forbidden 4f-4f transition. To experimentally evidence whether there is an energy transfer from STE to Nd^{3+} dopants, time-resolved PL (TRPL) spectra were collected on the Na/Bi/Nd:$Cs_2AgInCl_6$. TRPL spectra measured from 0 to 18.44 µs showed two kinds of emitting signals originating from STE emission (Figure 2g) and Nd^{3+} emission (Figure 2h) centered at 610 and 890 nm, respectively. With elongation of decay time, STE emission gradually decreases while Nd^{3+} emission remains unchanged (Figure S7, Supporting Information), suggesting no energy transfer from STE to Nd^{3+} dopants. This conclusion is further verified by that the decay lifetime for STE recombination exhibits no marked variation after Nd^{3+} doping (Figures S8 and S9, Supporting Information).

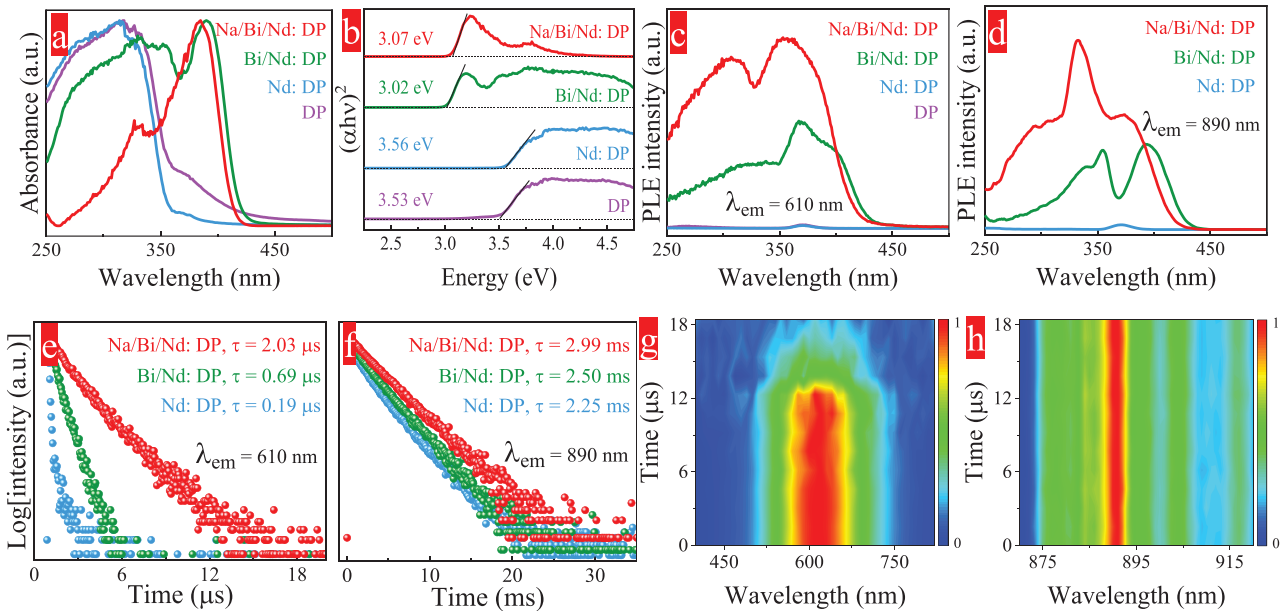

Figure 2. a) Absorption spectra, b) Tauc plots, c,d) PLE spectra, and e,f) PL decay curves by monitoring STE (610 nm) and Nd^{3+} (890 nm) emissions for the Nd^{3+} doped, Bi^{3+}/Nd^{3+} co-doped, and $Na^{+}/Bi^{3+}/Nd^{3+}$ tri-doped $Cs_2AgInCl_6$ samples. TRPL spectra of g) STE and h) Nd^{3+} emissions in the $Na^{+}/Bi^{3+}/Nd^{3+}$ tri-doped $Cs_2AgInCl_6$ sample with delayed time from 0 to 18.44 μs.

We further recorded temperature-dependent emission spectra to clarify the photophysical mechanism of the Nd:$Cs_2AgInCl_6$ and Na/Bi/Nd:$Cs_2AgInCl_6$. PL intensities of both STE and Nd^{3+} gradually decrease with elevation of temperature (**Figure 3**a,b) and the decay lifetimes monotonously shorten (Figure S10, Supporting Information). PL decays of STE in the temperature range of 20~320K remain on a μs scale (Figure S10a, Supporting Information), which is different from the case of isolated Bi^{3+} emission with an obvious decrease of decay lifetime from millisecond at 10 K to microsecond at 300 K owing to the occurrence of $^3P_0 \rightarrow {}^1S_0$ forbidden transition at low temperature.[18] Importantly, Na/Bi/Nd:$Cs_2AgInCl_6$ exhibits more stable luminescence for both STE recombination (Figure 3c,d) and Nd^{3+} NIR transition (Figure 3e) relative to that of Nd:$Cs_2AgInCl_6$ counterpart with the increase of temperature and the PL quenching tendency induced by temperature is significantly suppressed after Na^{+}/Bi^{3+} alloying. The exciton binding energy of the Nd^{3+}-doped and $Na^{+}/Bi^{3+}/Nd^{3+}$ tri-doped samples was calculated by fitting the Arrhenius equation.[19]

$$I(T) = \frac{I_0}{1 + A\exp\left(\frac{E_b}{k_B T}\right)} \quad (1)$$

where I_0, k_B, A, and E_b represent the integrated PL intensity at 0 K, Boltzmann constant, fitting constant, and exciton binding energy. The fitted results show that E_b values are determined to be 81.0 meV for the Nd^{3+} doped DP (Figure 3c) and 304.9 meV for the $Na^{+}/Bi^{3+}/Nd^{3+}$ tri-doped DP (Figure 3d). The remarkable increase of E_b implies that Na^{+}/Bi^{3+} co-alloying can effectively reduce recombination loss and thermal quenching of both STE and Nd^{3+} emissions (Table S5, Supporting Information).[20] Furthermore, the Huang–Rhys factor (S) is a dimensionless value that reflects the electron-phonon coupling strength, and S can be determined by fitting temperature-sensitive full width at half-maximum (FWHM) with the following equation.[21]

$$FWHM(T) = 2.36\sqrt{S}\,\hbar\omega_{phonon}\sqrt{\coth\frac{\hbar\omega_{phonon}}{2k_B T}} \quad (2)$$

where $\hbar\omega$ represents average phonon energy (effective vibrational energy). The S and $\hbar\omega$ were calculated to be 118.7 and 20.0 meV for the Nd:$Cs_2AgInCl_6$ DP and 37.7 and 35.2 meV for the Na/Bi/Nd: $Cs_2AgInCl_6$ sample (Figure 3f), respectively. In addition, the Fröhlich longitudinal optical phonon broadening model is used to get information on electron–phonon interactions.[22]

$$\Gamma(T) = \Gamma_0 + \Gamma_{LO}/\left(e^{\eta\omega_{LO}/k_B T} - 1\right) \quad (3)$$

here, Γ_0, Γ_{LO}, and $\eta\omega_{LO}$ are temperature-dependent broadening, exciton-optical phonon interaction, and optical phonon energy, respectively. The fitted results show that the values of Γ_0, Γ_{LO}, and $\eta\omega_{LO}$ decrease from 558.0 to 473.8, 1088.0 to 112.5, and 38.5 to 12.0 meV, respectively, after Na^{+}/Bi^{3+} co-doping (Figure S11 and Table S6, Supporting Information). Generally, the stronger the electron-phonon coupling, the larger the lattice relaxation (ΔR).[20a,23] It means that carriers in the excited state can undergo non-radiative recombination back to the ground state by thermally stimulated cross-over, reducing PL intensity. In addition, assuming that the ground state and excited state have similar phonon frequencies, the enhancement of effective phonon frequency will narrow the shape of the excited state curve and inhibit thermally induced cross-over quenching (Note S1, Supporting Information).[20b,24] All these results verify that Na^{+}/Bi^{3+} co-alloying can prevent the temperature quenching

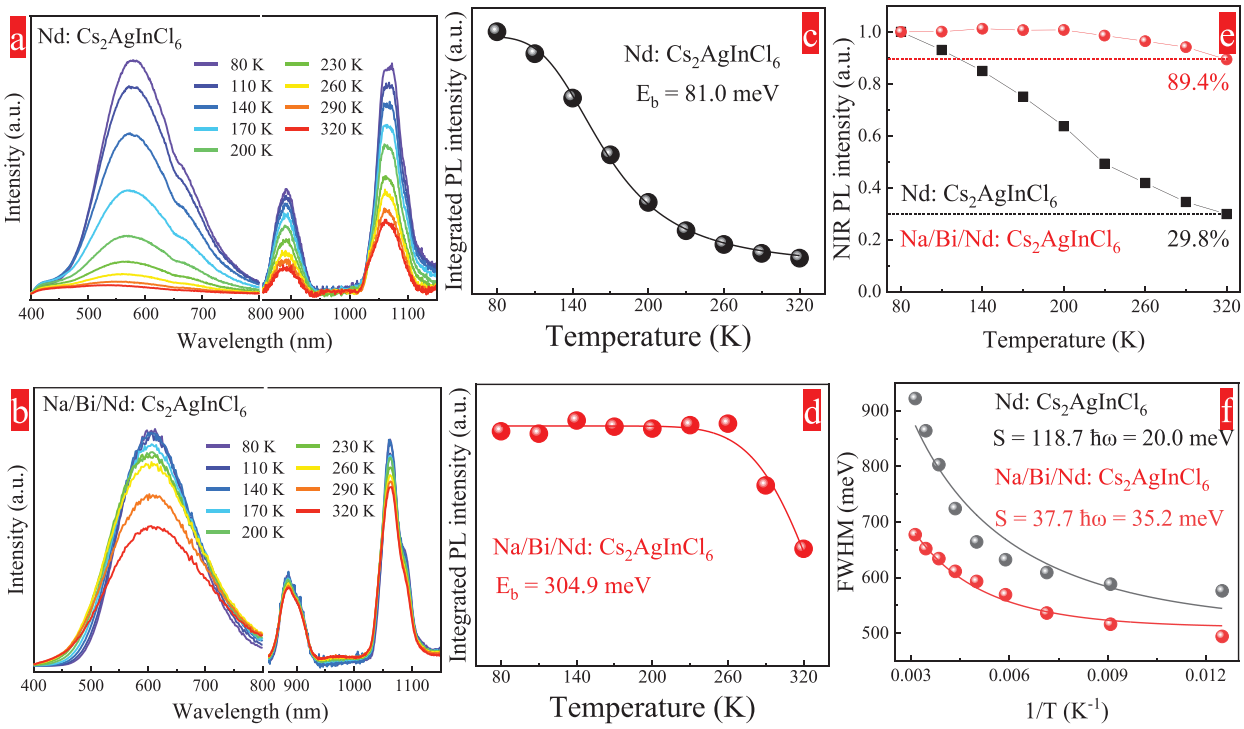

Figure 3. a,b) Temperature-dependent (≈80 to 320 K) PL spectra of Nd^{3+} doped and $Na^{+}/Bi^{3+}/Nd^{3+}$ tri-doped $Cs_2AgInCl_6$ DPs. The corresponding c,d) integrated STE PL intensities, e) Nd^{3+} NIR PL intensities, and f) FWHMs versus temperatures.

of both STE and Nd^{3+} emissions caused by strong electron-phonon coupling. Indeed, a less pronounced temperature broadening of both STE and Nd^{3+} PL spectral profiles is evidenced for the Na/Bi/Nd:$Cs_2AgInCl_6$ owing to the reduced electron-phonon coupling interaction (Figure S12, Supporting Information).

Furthermore, structural variations of Nd: $Cs_2AgInCl_6$ after Na^{+}/Bi^{3+} alloying were explored via DFT calculations based on a $\sqrt{2} \times \sqrt{2} \times 2$ supercell. The calculated electronic structures and projected density of states (DOS) are shown in Figure S13, Supporting Information. The valence band maximum (VBM) is predominantly composed of the Cl-3p and Ag-4d orbitals, and the conduction band minimum (CBM) is dominated by Cl-3p and In-5s orbitals. It is found that both Na^{+} and Bi^{3+} negligibly contribute to the VBM and CBM. To further investigate the role of dopants for the enhanced STE and Nd^{3+} NIR emissions on an atomic scale, more charge-density and geometry optimization calculations are implemented (**Figure 4**a–c). For Nd:$Cs_2AgInCl_6$, the electrons are strongly confined in $[InCl_6]^{3-}$ octahedrons in full real space, and the holes are localized around $[AgCl_6]^{5-}$ octahedrons, especially distributed in the surrounding Cl^{-} anions (Figure 4a). The introduced $[BiCl_6]^{3-}$ octahedrons will further aggravate the local distortion of $[AgCl_6]^{5-}$ octahedrons and decrease the electronic dimensionality of DP (Figure 4b). Moreover, the substitution of $[AgCl_6]^{5-}$ octahedrons by $[NaCl_6]^{5-}$ ones leads to more obvious spatial confinement of STE state, where electrons and holes are localized around the neighboring $[InCl_6]^{3-}$ and $[AgCl_6]^{5-}$ octahedrons, respectively (Figure 4c). This certainly benefited the formation of the trapped excitons owing to the enhanced overlapping between the electron and hole orbitals. We carried out fs-TA spectroscopic measurements on the Na/Bi/Nd:$Cs_2AgInCl_6$ sample to confirm the formation of STEs and explore the ultrafast kinetic processes. The contour plot of the fs-TA spectra shows a positive photoinduced absorption (PIA) in the detecting range from 430 to 700 nm (Figure 4d), indicating the generation of STEs in the DP crystal.[25] Furthermore, PIA dynamic traces in the ≈480 to 680 nm probing range exhibited the same rising time of 550 fs (Figure 4e,f), being close to the STE formation time reported previously.[25a,26] PIA decay curve at 580 nm and the corresponding biexponential fitting result are shown in Figure 4g. There are two different decay components: a fast decay with the fitted lifetime of 45.2 ps assigned to the nonradiative deexcitation of STEs to the quenching sites such as surface defects as well as lattice sites to produce phonons, and a slow decay with the fitted lifetime of 1015.6 ps ascribed to the radiative recombination of STEs to emit photons. Importantly, the percentage of nonradiative deexcitation (2.18%) was much lower than that of radiative transition (97.82%). These results unambiguously demonstrate that highly efficient radiative recombination process of STEs in the present $Na^{+}/Bi^{3+}/Nd^{3+}$ tri-doped $Cs_2AgInCl_6$.

The behaviors of lattice distortion in the DP sample after alloying were also investigated, as exhibited in **Figure 5**a. The introduced Nd^{3+}, Bi^{3+}, and Na^{+} contents will exacerbate the sublattice distortion of $[AgCl_6]^{5-}$ and $[NaCl_6]^{5-}$ octahedrons, while $[InCl_6]^{3-}$, $[BiCl_6]^{3-}$, and $[NdCl_6]^{3-}$ remain high local O_h site symmetry (Table S7, Supporting Information). In detail, Ag–Cl bond length depends critically on the nearest neighboring Bi^{3+}, which is much shorter (2.693 Å) than the average Ag-Cl (2.777 Å) bond length. The lattice distortion of $[AgCl_6]^{5-}$ octahedron will be further exacerbated when the STE state is formed.

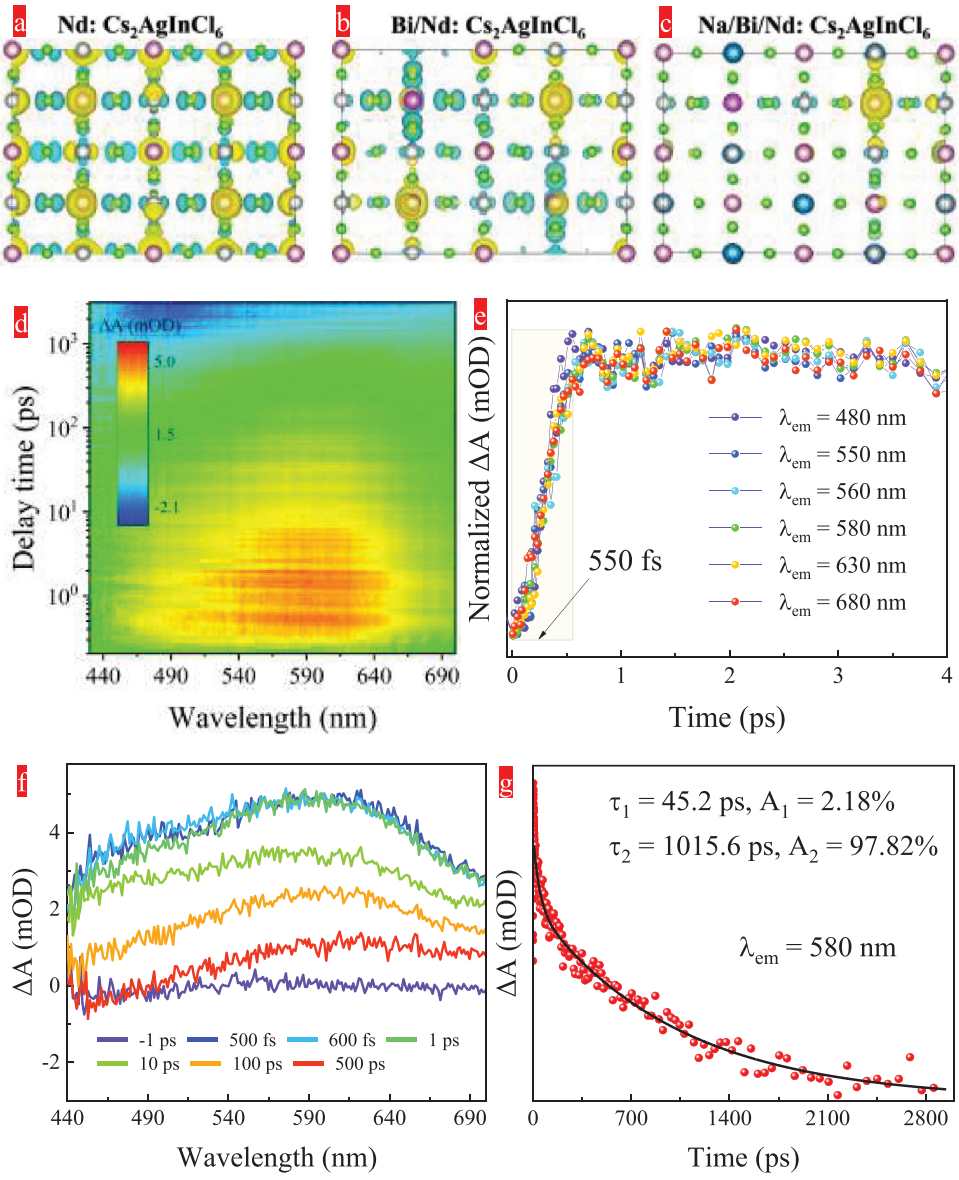

Figure 4. STE in a) Nd^{3+} doped, b) Bi^{3+}/Nd^{3+} co-doped, and c) $Na^{+}/Bi^{3+}/Nd^{3+}$ tri-doped $Cs_2AgInCl_6$ DPs. d) Contour plot of the fs-TA spectra of $Na^{+}/Bi^{3+}/Nd^{3+}$ tri-doped $Cs_2AgInCl_6$ under 360 nm fs laser excitation. e) The rising curves of normalized PIA kinetic data in the probe region from 480 to 680 nm. f) TA spectra within the set delay time values from 0.5 to 500 ps and g) PIA decay curve at 580 nm.

Moreover, Na^{+} doping will further reduce the local O_h symmetry of $[AgCl_6]^{5-}$ octahedron (Table S7, Supporting Information), which provides intuitive evidence of the breakdown of local site symmetry in the Na/Bi/Nd:$Cs_2AgInCl_6$ DP and promote the absorption/excitation of DP host and Nd^{3+} NIR-PLQY improvement. Importantly, the influence of electron-phonon coupling interaction is attenuated owing to the separation of the $[AgCl_6]^{5-}$ octahedrons by $[NaCl_6]^{5-}$ ones, which is consistent with the experimental data shown in Figure 3. To experimentally evidence the variation of the local environment after Na^{+}/Bi^{3+} doping, Raman spectra were measured under 532 nm laser excitation (Figure 5b). Raman spectrum of Nd:$Cs_2AgInCl_6$ consists of three Raman modes (A_{1g}, E_g, and T_{2g}).[20a,27] A_{1g} and E_g are assigned to symmetric and asymmetric stretching vibrations of $[AgCl_6]^{5-}$ and $[InCl_6]^{5-}$ octahedra, and T_{2g} corresponds to the translation motion of the Cs atom in the cuboctahedral cavity. With the addition of Na^{+} and Bi^{3+} dopants, the intensities of A_{1g} and E_g modes weaken owing to the decreased contents of $[AgCl_6]^{5-}$ and $[InCl_6]^{5-}$ octahedrons. Furthermore, the shifting of the Raman signals after Na^{+}/Bi^{3+} alloying confirms the occurrence of sublattice distortion induced by the replacement of $[InCl_6]^{5-}$ and $[AgCl_6]^{5-}$ octahedrons by $[BiCl_6]^{5-}$ and $[NaCl_6]^{5-}$ ones (Figure 5c).

Accordingly, a possible photophysical mechanism that describes the simultaneous enhancement of STE broadband luminescence and Nd^{3+} NIR emissions in the Na/Bi/Nd:$Cs_2AgInCl_6$ DP is proposed. According to DFT calculations, both VBM and CBM of $Cs_2AgInCl_6$ locate at the Γ point (Figure S13, Supporting Information). As schematically illustrated in Figure 5d, Γ_{3+},

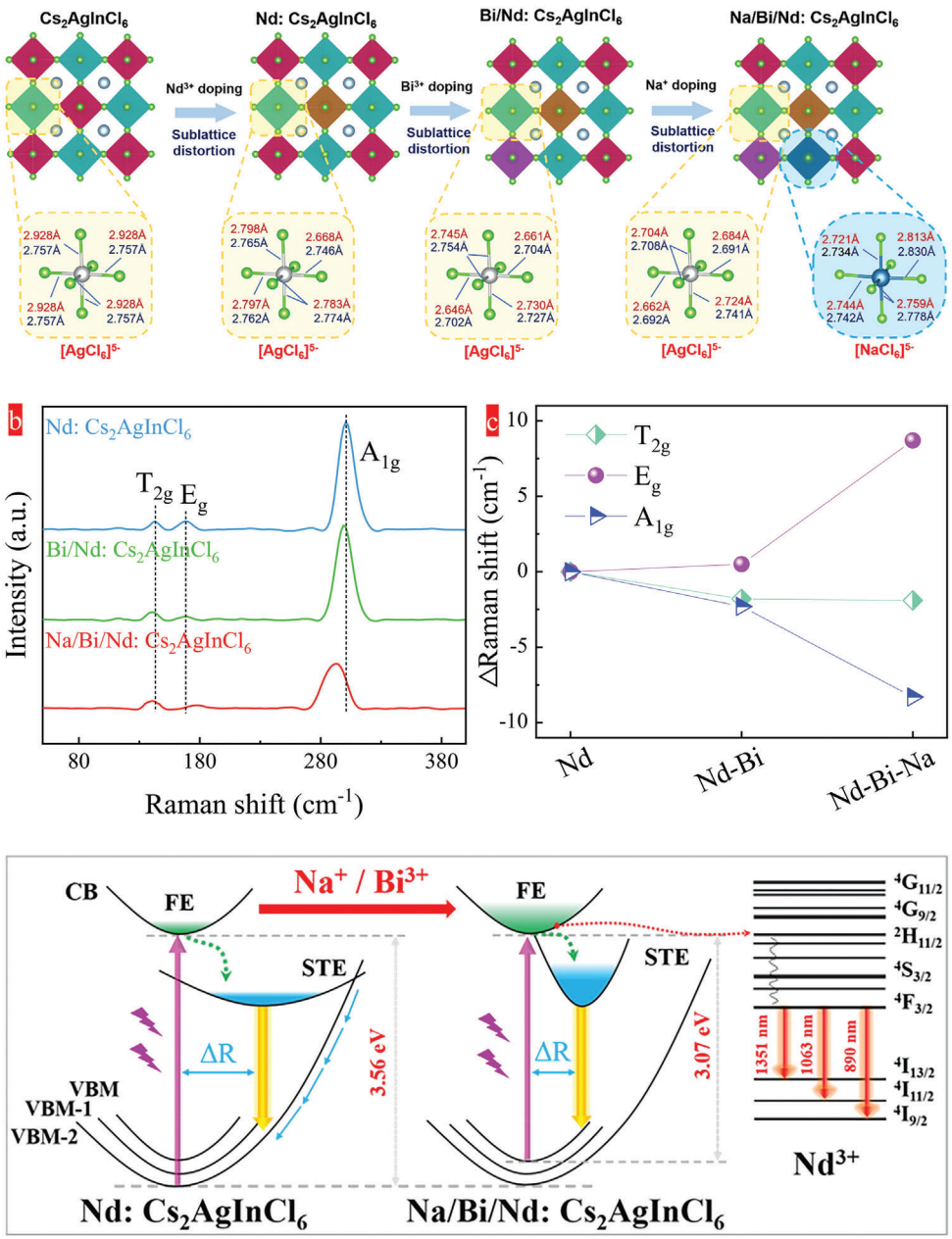

Figure 5. a) Schematic diagram of sublattice distortion in $Cs_2InAgCl_6$ caused by Nd^{3+}, Bi^{3+}, and Na^+ doping. Red, cyan, orange, purple, and blue octahedrons represent $[InCl_6]^{3-}$, $[AgCl_6]^{5-}$, $[NdCl_6]^{3-}$, $[BiCl_6]^{3-}$, and $[NaCl_6]^{5-}$, respectively. Blue and red color data represent the bond length in $[AgCl_6]^{5-}$ and $[NaCl_6]^{5-}$ octahedrons at the ground state and the excited state, respectively. b) Raman spectra of Nd^{3+} doped, Bi^{3+}/Nd^{3+} co-doped, and $Na^+/Bi^{3+}/Nd^{3+}$ tri-doped $Cs_2AgInCl_6$ samples. c) Relative Raman peaks shift relative to the respective peak positions of Nd:$Cs_2AgInCl_6$. d) Proposed photophysical processes in the Nd^{3+} doped and $Na^+/Bi^{3+}/Nd^{3+}$ tri-doped $Cs_2AgInCl_6$ DPs involving both STE recombination and Nd^{3+} 4f-4f transitions via free exciton sensitization.

Γ_{4+}, and Γ_{4-} are used to denote VBM, VBM-1, and VBM-2 states, respectively, and Γ_{1+} represents the first conduction-band state. Evidently, Γ_{3+} and Γ_{4+} have the same parities as Γ_{1+}, while Γ_{4-} has the opposite parity relative to Γ_{1+}.[16,28] Therefore, it can be concluded that VBM&VBM-1 to CBM transitions are forbidden and VBM-2 to CBM transition is allowed. In this case, the detected optical bandgap of 3.56 eV of the Nd:$Cs_2AgInCl_6$ sample is assigned to the parity-allowed VBM-2 to CBM transition. Generally, there are two possible routes to transfer energy to Ln^{3+} dopants in the DP samples: one is energy transfer from STE to Ln^{3+} and the other is energy transfer from free exciton to Ln^{3+}. The former will lead to the quenching of STE emission, while the latter will not. In the present Nd^{3+}-doped case, both TRPL spectra and decay curves of STE recombination (Figure 2g,h, and Figures S7–S9, Supporting Information) exclude the possibility of energy transfer from STE to Nd^{3+} dopants. PLE spectra by monitoring

STE emission and Nd^{3+} NIR emission (Figure 2c,d) clearly evidence the occurrence of energy transfer from free exciton to STE and Nd^{3+} dopants. Therefore, the excitation of STE and Nd^{3+} is mainly ascribed to energy transfer from the VBM to CBM transition, which explains the weak emissions of STE and Nd^{3+} due to the parity-forbidden transition between VBM and CBM for the $Nd:Cs_2AgInCl_6$ sample. Bi^{3+} alloying breaks the parity-forbidden transitions from VBM and VBM-1 to CBM. This leads to strong absorption/excitation of VBM to CBM transition, and the formed free excitons can be effectively transferred to both STE and Nd^{3+}, which can significantly enhance STE and Nd^{3+} NIR emissions. Further incorporation of Na^+ ions plays the role of acting as a hindrance to separate the connections among $[AgCl_6]^{5-}$ octahedra to localize STEs and weaken electron-phonon coupling interactions. As a consequence, the exciton binding energy increases after Na^+ alloying, which is beneficial to reducing thermal quenching of STE luminescence at room temperature and leading to more excitons in the self-trapped state shown in Figure 5d. In addition, the weakening electron-phonon coupling results in reducing the ΔR and inhibits the thermally induced crossover between the excited state and ground state in the configurational coordinate diagram, leading to efficient luminescence at room temperature. Finally, Na^+ doping can further distort $[AgCl_6]^{5-}$ octahedrons and break parity-forbidden transitions from VBM and VBM-1 to CBM. This leads to the formation of more FEs via strong UV light excitation, which can be efficiently transferred to both STE and Nd^{3+} and lead to simultaneous enhancement of STE broadband luminescence and Nd^{3+} NIR emissions.

Furthermore, we evaluated the stability of $Na/Bi/Nd:Cs_2AgInCl_6$ DP. As shown in Figure S14a, Supporting Information, the thermogravimetric (TG) curve shows that the $Nd:Cs_2AgInCl_6$ sample tends to be stable below 464 °C, and a further increase in temperature leads to gradual thermal decomposition of DP. Importantly, incorporation of Na^+/Bi^{3+} increases thermal decomposition temperature up to 549 °C (Figure S14a, Supporting Information), and NIR PL intensity remains unchanged relative to the initial one after cooling/heating (320–140–320 K) (Figure S14b, Supporting Information), indicating that Na^+/Bi^{3+} co-alloying is beneficial to improvement of structural stability of the $Nd:Cs_2AgInCl_6$ DP. Moreover, after exposure to ambient air for 180 days, no obvious change in structure and PL spectra is detected (Figure S14c,d, Supporting Information), confirming superior environmental stability of the present $Na/Bi/Nd:Cs_2AgInCl_6$ material.

The $Na/Bi/Nd:Cs_2AgInCl_6$ DP exhibits superior stability, high PLQY, and yellow STE emission and multi-wavelength Nd^{3+} NIR emissions under UV light excitation, making its promise for the usage as vis–NIR dual-emitters in diverse advanced fields. We prepared the phosphor-converted LED (pc-LED) by coupling the as-prepared DPs-polydimethylsiloxane (DPs@PDMS) film (Figure S15a,b, Supporting Information) with a commercial UV chip. The PL intensity of the constructed pc-LED (100 mW) after continuous operation for 48 h shows only slight PL thermal quenching (Figure S15c, Supporting Information). The pc-LED produces bright yellow light to the naked eye and intense NIR light detectable by a NIR camera (Figure S16a, Supporting Information). To demonstrate the penetration of pc-LED in tissues, we took three different tissue sections from the same piece of pork, each ≈3 mm thick. The remained intensities after penetrating lean flesh, fat-meat, and skin were 36.3%, 43.8%, and 15.3%, respectively (Figure S16b, Supporting Information). The residual intensity could reach 2.5% after stacking the three tissues together. Figure S17, Supporting Information shows the remaining emitting intensities after passing through the corresponding tissues recorded by the visible camera and NIR camera, respectively. It indicates that we can discern different biological tissues based on the ratio of residual intensity to the initial one after penetration. In addition, benefiting from the intense NIR emitting feature of the present pc-LED, it is demonstrated that NIR light can penetrate plastic containers but is absorbed by the cleaning agent in the container (Figure S16c-i,ii, Supporting Information) and can also be used to distinguish and identify different liquids, such as water and cola (Figure S16c iii–v, Supporting Information). The NIR light can pass through water but is completely absorbed by cola. Figure S16d, Supporting Information shows photographs of succulents and fruits recorded by visible and NIR cameras. No signal can be detected when the pc-LED is off. When the pc-LED is lightened, the colorful and black and white photographs were recorded by visible and NIR cameras, respectively. These phenomena confirm that pc-LED device based on $Na/Bi/Nd:Cs_2AgInCl_6$ DP material has great potential in applications such as spectral analysis, imaging, and night vision.

3. Conclusion

In summary, we have developed a new type of visible-NIR phosphors based on the efficient sensitization of both STE and Nd^{3+} via free excitons in the Na^+/Bi^{3+} co-alloyed $Nd:Cs_2AgInCl_6$ DPs. By virtue of Na^+/Bi^{3+} doping, both bright broadband luminescence originating from STE recombination and intense NIR emissions ascribing to the 4f-4f transitions of Nd^{3+} were realized, with NIR PLQY up to 30.3%. The underlying PL process and energy transfer mechanism were comprehensively studied through optical spectroscopy and DFT calculations, which verified that the significantly improved STE and Nd^{3+} emissions mainly benefited from the synergistic effect of Na^+/Bi^{3+}-induced modification of local site symmetry, breakdown of parity-forbidden absorption, and reduction of electron-phonon coupling. In addition, the $Na^+/Bi^{3+}/Nd^{3+}$ tri-doped $Cs_2AgInCl_6$ DP exhibited superior environmental stability and can be used to construct pc-LED, showing practical applications in spectral analysis, imaging, and night vision. These findings provide fundamental insights into the design of efficient Ln^{3+}-doped DPs covering both visible and NIR spectral ranges for versatile optoelectronic applications.

Supporting Information

Supporting Information is available from the Wiley Online Library or from the author.

Acknowledgements

This research was supported by the National Key Research and Development Program of China (2021YFB3500503), National Natural Science Foundation of China (52272141, 51972060, 12074068, 52102159,

and 22103013), the Fujian Science & Technology Innovation Laboratory for Optoelectronic Information (2021ZZ126), and the Natural Science Foundation of Fujian Province (2020J02017, 2021J06021, 2021J01190, and 2020J01931).

Conflict of Interest

The authors declare no conflict of interest.

Data Availability Statement

Research data are not shared.

Keywords

double perovskites, lanthanides, light-emitting diodes, luminescent materials, near-infrared emissions

Received: April 25, 2023
Revised: July 28, 2023
Published online:

[1] a) Y. Zorenko, J. Mares, R. Kucerkova, V. Gorbenko, V. Savchyn, T. Voznyak, M. Nikl, A. Beitlerova, K. Jurek, *J. Phys. D: Appl. Phys.* **2009**, *42*, 075501; b) V. Babin, V. Gorbenko, A. Krasnikov, A. Makhov, E. Mihokova, M. Nikl, S. Zazubovich, Y.u. Zorenko, *Phys. Status Solidi B* **2012**, *249*, 1039; c) H. Arfin, A. Kshirsagar, J. Kaur, B. Mondal, Z. Xia, S. Chakraborty, A. Nag, *Chem. Mater.* **2020**, *32*, 10255; d) H. Arfin, A. Nag, *J. Phys. Chem. Lett.* **2021**, *12*, 10002.

[2] a) V. Rajendran, M. H. Fang, G. N. De Guzman, T. Lesniewski, S. Mahlik, M. Grinberg, G. Leniec, S. M. Kaczmarek, Y. S. Lin, K. M. Lu, C. M. Lin, H. Chang, S. F. Hu, R. S. Liu, *ACS Energy Lett.* **2018**, *3*, 2679; b) Z. W. Jia, C. X. Yuan, Y. F. Liu, X. J. Wang, P. Sun, L. Wang, H. C. Jiang, J. Jiang, *Light: Sci. Appl.* **2020**, *9*, 86; c) S. He, L. L. Zhang, H. Wu, H. J. Wu, G. H. Pan, Z. D. Hao, X. Zhang, L. G. Zhang, H. Zhang, J. H. Zhang, *Adv. Opt. Mater.* **2020**, *8*, 1901684. d) M. H. Fang, K. C. Chen, N. Majewska, T. Lesniewski, S. Mahlik, G. Leniec, S. M. Kaczmarek, C. W. Yang, K. M. Lu, H. S. Sheu, R. S. Liu, *ACS Energy Lett.* **2021**, *6*, 109.

[3] S. F. Zhou, N. Jiang, B. Zhu, H. C. Yang, S. Ye, G. Lakshminarayana, J. H. Hao, J. R. Qiu, *Adv. Funct. Mater.* **2008**, *18*, 1407.

[4] R. Marin, D. Jaque, *Chem. Rev.* **2021**, *121*, 1425.

[5] a) Z. K. Tan, R. S. Moghaddam, M. L. Lai, P. Docampo, R. Higler, F. Deschler, M. Price, A. Sadhanala, L. M. Pazos, D. Credgington, *Nat. Nanotechnol.* **2014**, *9*, 687; b) J. Lin, Y. Lu, X. Li, F. Huang, C. Yang, M. Liu, N. Jiang, D. Chen, *ACS Energy Lett.* **2021**, *6*, 519; c) S. Liao, Z. Yang, J. Lin, S. Wang, J. Zhu, S. Chen, F. Huang, Y. Zheng, D. Chen, *Adv. Funct. Mater.* **2023**, *33*, 2210558; d) S. Chen, J. Lin, S. Zheng, Y. Zheng, D. Chen, *Adv. Funct. Mater.* **2023**, *33*, 2213442.

[6] a) C. Otero-Martínez, J. Ye, J. Sung, I. Pastoriza-Santos, J. Pérez-Juste, Z. Xia, A. Rao, R. L. Hoye, L. Polavarapu, *Adv. Mater.* **2022**, *34*, 2107105; b) C.-Y. Huang, H. Li, Y. Wu, C.-H. Lin, X. Guan, L. Hu, J. Kim, X. Zhu, H. Zeng, T. Wu, *Nano–Micro Lett.* **2023**, *15*, 16; c) W. Zhou, Y. Shen, L. X. Cao, Y. Lu, Y. Y. Tang, K. Zhang, H. Ren, F. M. Xie, Y. Q. Li, J. X. Tang, *Adv. Funct. Mater.* **2023**, *33*, 2301425.

[7] a) X. Shen, K. Kang, Z. Yu, W. H. Jeong, H. Choi, S. H. Park, S. D. Stranks, H. J. Snaith, R. H. Friend, B. R. Lee, *Joule* **2023**, *7*, 272; b) Y. Yu, Y. Tang, B. Wang, K. Zhang, J. X. Tang, Y. Q. Li, *Laser Photonics Rev.* **2023**, *17*, 2200608.

[8] a) G. Pan, X. Bai, D. Yang, X. Chen, P. Jing, S. Qu, L. Zhang, D. Zhou, J. Zhu, W. Xu, *Nano Lett.* **2017**, *17*, 8005; b) H. Li, X. Liu, D. Zhou, B. Dong, L. Xu, X. Bai, H. Song, *Adv. Mater.* **2023**, *35*, 2300118.

[9] a) Y. J. Yu, C. Zou, W. S. Shen, X. Zheng, Q. S. Tian, Y. J. Yu, C. H. Chen, B. Zhao, Z.-K. Wang, D. Di, *Angew. Chem., Int. Ed.* **2023**, *62*, 202302005; b) X. Shen, Z. Wang, C. Tang, X. Zhang, B. R. Lee, X. Li, D. Li, Y. Zhang, J. Hu, D. Zhao, *Nano Lett.* **2023**, *23*, 82.

[10] a) H. Tang, Y. Xu, X. Hu, Q. Hu, T. Chen, W. Jiang, L. Wang, W. Jiang, *Adv. Sci.* **2021**, *8*, 2004118; b) Y. Wu, X. Li, H. Zeng, *Small Struct.* **2021**, *2*, 2000071; c) Y. Liu, X. Rong, M. Li, M. S. Molokeev, J. Zhao, Z. Xia, *Angew. Chem., Int. Ed.* **2020**, *59*, 11634; d) S. Saikia, A. Joshi, H. Arfin, S. Badola, S. Saha, A. Nag, *Angew. Chem., Int. Ed.* **2022**, *61*, 202201628.

[11] Y. Liu, A. Nag, L. Manna, Z. Xia, *Angew. Chem., Int. Ed.* **2021**, *133*, 11696.

[12] a) W. Lee, S. Hong, S. Kim, *J. Phys. Chem. C* **2019**, *123*, 2665; b) H. Arfin, J. Kaur, T. Sheikh, S. Chakraborty, A. Nag, *Angew. Chem., Int. Ed.* **2020**, *59*, 11307.

[13] a) L. Cao, X. Jia, W. Gan, C. G. Ma, J. Zhang, B. Lou, J. Wang, *Adv. Funct. Mater.* **2023**, *33*, 2212135; b) N. Liu, W. Zheng, R. Sun, X. Li, X. Xie, L. Wang, Y. Zhang, *Adv. Funct. Mater.* **2022**, *32*, 2110663; c) J. Sun, W. Zheng, P. Huang, M. Zhang, W. Zhang, Z. Deng, S. Yu, M. Jin, X. Chen, *Angew. Chem., Int. Ed.* **2022**, *61*, 202201993.

[14] a) J. Zhao, G. Pan, Y. Zhu, K. Liu, W. You, X. Chen, H. Song, Y. Mao, *ACS Appl. Mater. Interfaces* **2022**, *14*, 42215; b) G. Yang, S. Bai, X. Li, H. Liang, C. Li, J. Sun, Y. Wang, J. Huang, G. Pan, Y. Zhu, *ACS Appl. Mater. Interfaces* **2023**, *15*, 24629.

[15] a) S. Jin, R. Li, H. Huang, N. Jiang, J. Lin, S. Wang, Y. Zheng, X. Chen, D. Chen, *Light: Sci. Appl.* **2022**, *11*, 52; b) S. Jin, R. Li, J. Zhu, T. Pang, T. Wu, H. Zhan, Y. Zheng, F. Huang, X. Chen, D. Chen, *Mater. Horiz.* **2023**, *10*, 1406.

[16] J. Zhou, Z. Xia, M. S. Molokeev, X. Zhang, D. Peng, Q. Liu, *J. Mater. Chem. A* **2017**, *5*, 15031.

[17] J. Luo, X. Wang, S. Li, J. Liu, Y. Guo, G. Niu, L. Yao, Y. Fu, L. Gao, Q. Dong, C. Zhao, M. Leng, F. Ma, W. Liang, L. Wang, S. Jin, J. Han, L. Zhang, J. Etheridge, J. Wang, Y. Yan, E. H. Sargent, J. Tang, *Nature* **2018**, *563*, 541.

[18] M. Jin, W. Zheng, Z. Gong, P. Huang, R. Li, J. Xu, X. Cheng, W. Zhang, X. Chen, *Nano Res.* **2022**, *15*, 6422.

[19] Z. Chen, C. Yu, K. Shum, J. J. Wang, W. Pfenninger, N. Vockic, J. Midgley, J. T. Kenney, *J. Lumin.* **2012**, *132*, 345.

[20] a) X. Cheng, Z. Xie, W. Zheng, R. Li, Z. Deng, D. Tu, X. Shang, J. Xu, Z. Gong, X. Li, *Adv. Sci.* **2022**, *9*, 2103724; b) G. Zhang, D. Wang, B. Lou, C. G. Ma, A. Meijerink, Y. Wang, *Angew. Chem., Int. Ed.* **2022**, *61*, 202207454.

[21] W. Stadler, D. Hofmann, H. Alt, T. Muschik, B. Meyer, E. Weigel, G. Müller-Vogt, M. Salk, E. Rupp, K. Benz, *Phys. Rev. B* **1995**, *51*, 10619.

[22] S. Rudin, T. Reinecke, B. Segall, *Phys. Rev. B* **1990**, *42*, 11218.

[23] G. Blasse, in *Advances in Inorganic Chemistry*, (Ed: A. G. Sykes), Vol. *35*, Academic Press, United States **1990**, p. 319.

[24] Y. Jia, S. Poncé, A. Miglio, M. Mikami, X. Gonze, *J. Lumin.* **2020**, *224*, 117258.

[25] a) B. Yang, X. Mao, F. Hong, W. Meng, Y. Tang, X. Xia, S. Yang, W. Deng, K. Han, *J. Am. Chem. Soc.* **2018**, *140*, 17001; b) M. Cong, B. Yang, F. Hong, T. Zheng, Y. Sang, J. Guo, S. Yang, K. Han, *Sci. Bull.* **2020**, *65*, 1078.

[26] F. Jiang, Z. N. Wu, M. Lu, Y. Gao, X. Li, X. Bai, Y. Ji, Y. Zhang, *Adv. Mater.* **2023**, 2211088, https://doi.org/10.1002/adma.202211088.

[27] H. Siddique, Z. Xu, X. Li, S. Saeed, W. Liang, X. Wang, C. Gao, R. Dai, Z. Wang, Z. Zhang, *J. Phys. Chem. Lett.* **2020**, *11*, 9572.

[28] Y. Liu, Y. Jing, J. Zhao, Q. Liu, Z. Xia, *Chem. Mater.* **2019**, *31*, 3333.